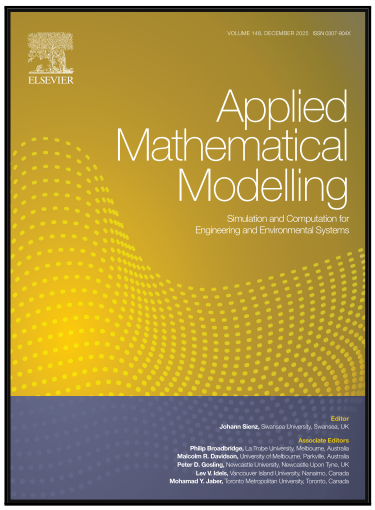

Meiotic oocyte spindle formation and separation dynamics predicted by Turing patterns

Yidi Zhang , Xiaoying Ye , Yuan Huang , Shan Guo , Yaowei Liu , Lin Liu , Xin Zhao

PII: S0307-904X(26)00363-X
DOI: https://doi.org/10.1016/j.apm.2026.117102
Reference: APM 117102

To appear in: *Applied Mathematical Modelling*

Received date: 6 December 2025
Revised date: 3 May 2026
Accepted date: 1 June 2026

Please cite this article as: Yidi Zhang , Xiaoying Ye , Yuan Huang , Shan Guo , Yaowei Liu , Lin Liu , Xin Zhao , Meiotic oocyte spindle formation and separation dynamics predicted by Turing patterns, *Applied Mathematical Modelling* (2026), doi: https://doi.org/10.1016/j.apm.2026.117102

Highlights

- Recorded the complete meiotic oocyte maturation process clearly without injecting any markers.
- Reproduced the spindle formation and separation processes based on the Turing secondary pattern theory.
- Validated the model through morphological and spatiotemporal characteristic analysis.
- Pioneered the assessment of model-experiment agreement through dynamic characteristics, introducing a novel method for Turing model validation.
- The predictions derived from this model effectively guided the biological experiments, providing a significant new perspective for the investigation of spindle development.

Meiotic oocyte spindle formation and separation dynamics predicted by Turing patterns

Yidi Zhang[1,¶], Xiaoying Ye[2,3,¶], Yuan Huang[1], Shan Guo[4], Yaowei Liu[1,5], Lin Liu[2,3,*], Xin Zhao[1,5,*]

[1] National Key Laboratory of Intelligent Tracking and Forecasting for Infectious Diseases, Engineering Research Center of Trusted Behavior Intelligence, Ministry of Education, Tianjin Key Laboratory of Intelligent Robotic (tjKLIR), Institute of Robotics and Automatic Information System (IRAIS), Nankai University, Tianjin, China

[2] State Key Laboratory of Medicinal Chemical Biology, Nankai University, Tianjin, China

[3] Department of Cell Biology and Genetics, College of Life Sciences, Nankai University, Tianjin, China

[4] College of Mathematics and Computer Science, Yan'an University, 716000, China

[5] Institute of Intelligence Technology and Robotic Systems, Shenzhen Research Institute of Nankai University, Shenzhen, China

[*] Corresponding authors: liulin@nankai.edu.cn (Lin Liu), zhaoxin@nankai.edu.cn (Xin Zhao).

[¶] These authors contributed equally to this work.

Abstract

Spindle formation and separation are critical for the accurate segregation of genetic material during cell division. Recently, we recorded the meiotic oocyte maturation process with high-resolution differential interference contrast microscopy, in which the process of spindle formation and separation can be observed without any labeling. From a morphological perspective, after germinal vesicle breakdown, a spindle-like structure gradually emerged within the oocyte, migrated to the cortex, and then rapidly split into two parts, accompanied by polar body extrusion. From a pattern formation perspective, this sequence can be viewed as the generation of a spindle-like pattern, followed by its transformation into a double-spindle-like pattern through division. In this study, we abstracted spindle formation and separation as the emergence of a single-spot primary Turing pattern and its subsequent transformation into a double-spot secondary Turing pattern, and simulated both processes using a Turing reaction-diffusion model. After mapping the simulation timeline to real-world time, the simulated results showed strong spatiotemporal agreement with the time-lapse imaging. No significant phase lag was observed. We then applied optical flow analysis to compare the dynamic characteristics of time-lapse imaging and numerical simulation. The results revealed a consistent trend: particle movement intensity increases markedly from the formation stage (single-spot pattern) to the separation stage (double-spot pattern). Finally, the model provided two predictions on the impact of increased inhibitory input on spindle separation, supported by cell experiments. These findings suggest that Turing reaction-diffusion principles may be involved in the regulation of spindle formation and separation.

Keywords: Reaction-diffusion model, Turing pattern, Pattern transformation, Spindle formation, Spindle separation, Optical flow.

1. Introduction

Spindle formation and separation are critical for the accurate segregation of genetic material during cell division [1, 2]. Recently, we recorded the meiotic oocyte maturation process with high-resolution differential interference contrast (DIC) microscopy, in which the process of spindle formation and separation can be observed without any labeling [3]. From a morphological perspective, the spindle gradually formed within the nearly structureless oocyte after germinal vesicle breakdown (GVBD). It then migrated to the oocyte cortex, rapidly dividing into two parts, accompanied by the extrusion of the polar body. Understanding this phenomenon has attracted significant attention from researchers [4-12]. However, the complex coupling among biological processes and current experimental limitations hinder a comprehensive understanding of spindle dynamics and spindle separation. Here, we adopted a mathematical model based on biological research to understand this problem from the perspective of biological patterns.

The reaction-diffusion model proposed by Turing in 1952 demonstrates that a system of interacting chemical substances (morphogens) can spontaneously generate stable, spatially non-uniform patterns, providing a theoretical basis for biological morphogenesis [13-16]. The model consists of two partial differential equations that describe the reaction-diffusion interactions between morphogens. Morphogens were subsequently divided into two types: one acting as activator and the other as inhibitor, which establish the primary pattern by auto- and cross-catalytic effects on the sources, spreading by diffusion or other mechanisms, and degradation [17]. The model could generate different patterns and has demonstrated the potential to explain the mechanisms of various morphological phenomena [18-22], such as the gorgeous patterning of feathers [18], the variety in vertebrate skin patterns [19], and the complex shell patterns of seashells [20]. Beyond morphogenesis, Turing instability analysis has also been

extended to a range of other systems, demonstrating the methodological generality of this framework [23-26]. Notably, the positioning of the bacterial cell division plane has been accurately modeled within the framework of the Turing model [27].

As Turing theory has advanced, Turing patterns have been classified into primary and secondary patterns. Beginning with a uniform distribution of morphogens, disturbances can induce instability in the system, which ultimately stabilizes into a specific spatial distribution referred to as a primary Turing pattern. Spindle formation, which morphologically changes from an initially uniform state to a spindle-like pattern, closely resembles the development of a primary Turing pattern. Pattern transformation has also been investigated based on Turing theory. Starting with a primary Turing pattern as the initial condition, certain parameter changes can destabilize the system, leading to a rapid transformation and eventually stabilizing into a new spatial configuration known as the secondary Turing pattern or secondary bifurcation pattern [16]. The secondary Turing patterns have been well demonstrated in describing denser stripe patterns formed by vascular mesenchymal cells due to the influence of drugs and the formation of lung branches and vascular branches [28-30]. In this study, the spindle rapidly divides into two parts upon reaching the oocyte cortex, a process that morphologically resembles the formation of a secondary Turing pattern.

This study employed the Turing reaction-diffusion model to investigate the complete developmental process of spindle formation and separation within oocytes based on the Turing secondary pattern theory. To obtain detailed biological information, we recorded the meiotic oocyte maturation process using high-resolution DIC microscopy without any labeling. We generated a single-spot primary pattern based on the reaction-diffusion model to simulate the spindle formation, and subsequently transformed the pattern into a double-spot secondary pattern to reproduce spindle separation by adjusting key parameters. The agreement between the numerical simulation and the time-lapse imaging was verified through morphological and spatiotemporal characteristic analysis. Next, we established a dynamic characteristic analysis method based on optical flow, revealing a consistent trend in particle movement intensity between the numerical simulation and the actual developmental process of the spindle in time-lapse imaging. Finally, the model provided two predictions: increased inhibitory input 1) prolongs spindle separation and 2) reduces the success of spindle separation, which were supported by cell experiments.

2. Materials and methods

2.1 Oocyte collection

The use of mice in this research was approved by the Nankai University Animal Care and Use Committee. All mice used in this study were cared for and operated on according to the relevant regulations. The mice were housed in individually ventilated cages (IVCs) on a standard 12 h light: 12 h dark cycle in the sterile Animal Facility at the College of Life Sciences. ICR mice (5 weeks old) were injected with 5 IU of PMSG, and GV oocytes were collected after 46 hours. Cumulus cells were gently removed by pipetting 0.06% hyaluronidase after IVM culture for 6 hours. The IVM medium consisted of 95% MEM, 5% FBS, 0.24 mM sodium pyruvate, 1.5 IU/ml human chorionic gonadotrophin (hCG) and 1 IU/ml PMSG.

2.2 Time-lapse DIC imaging

DIC imaging was performed using a Zeiss Axiovert 200M inverted microscope equipped with AxioCam MRm and AxioVision Rel. 4.4 software, which were used to acquire and analyze the time-lapse images, respectively [3]. The temperature was maintained at 37 °C by a Tempcontrol 37-2 digital in a plastic chamber (Zeiss). The voltage of the halogen lamp was set to the minimal level, and the light automatically turned on prior to capturing an image and turned off after the image was captured to minimize the oocyte's exposure to light to less than 260 ms. A 63X 1.4 N.A. oil Plan-Apochromat objective was used to capture the details of the chromosome dynamics. Microtubules and spindles of mouse oocytes were imaged using a Zeiss Axiovert 100 inverted microscope. Oocytes were imaged at 37 °C in HEPES (25 mM)-buffered maturation medium in a homemade chamber placed in a heated box on the microscope stage. Time-lapse images were captured every 2 or 4 min in most cases. To control for experimental variations among oocytes, particularly temperature and the time after oocyte collection, we imaged at least five oocytes in each treatment group on different days and presented two representative time-lapse videos.

2.3 Mathematical model

The mathematical model utilized in this study is a reaction-diffusion system widely applied to describe pattern formation phenomena in tissue differentiation, originally proposed by Gierer and Meinhardt in 1972 [17]. The model consists of a system of two partial differential equations, characterizing the reaction-diffusion interactions between the activator and inhibitor. Since the Gierer-Meinhardt model is designed to describe tissue differentiation, it accounts for cell density as a factor influencing pattern formation. Given that our study models intracellular processes within a single cell, we adapted the model accordingly, as shown in Equations (1-2):

$$\frac{\partial a}{\partial t} = D_a \nabla^2 a + \frac{c_a a^2}{h(1+ka^2)} - \mu_a a \tag{1}$$

$$\frac{\partial h}{\partial t} = D_h \nabla^2 h + c_h a^2 - \mu_h h + \mathrm{H} \tag{2}$$

The model includes diffusion terms $D_a\nabla^2 a$ and $D_h\nabla^2 h$, representing the free diffusion of activator and inhibitor according to their respective concentration gradients, where D_a and D_h denote the diffusion rates of the activator and inhibitor. The remaining terms in the equations represent the reaction terms, where $c_a a^2/h(1+ka^2)$ and $c_h a^2$ characterize the secretion mechanisms of the activator and inhibitor under their interactive influences. The parameters c_a and c_h correspond to the respective reaction rate constants for each term. Both terms are multiplied by a^2 to signify the facilitative role of the activator in the secretion of morphogens. However, this self-activation effect of the activator is saturable, which is expressed by including $(1+ka^2)$ in the denominator, where *k* denotes the autocatalytic saturation coefficient. The inhibition of *a* by *h* is modeled by placing the *h* term in the denominator. The reaction terms $\mu_a a$ and $\mu_h h$ represent the decay effects of the activator and inhibitor based on their own concentrations, with μ_a and μ_h as respective decay coefficients. *H* denotes an externally introduced inhibitor source, where *H*=0 in the absence of exogenous additions in the experiment.

To eliminate the influence of dimensional units on both mechanistic analysis and computational efficiency, Equations (1-2) are subjected to nondimensionalization. This process establishes parameter correspondences between the dimensional and dimensionless models, aiming to identify essential biological parameters and reduce the overall parameter complexity. Here, following the nondimensionalization approach presented by Alan Garfinkel et al. in Reference 28, we nondimensionalized the model (Equations (1-2)) by setting $D=D_a/D_h$ and $\gamma=L^2\gamma^*/D_h$ (where $\gamma^*=T^{-1}$, *L* and *T* are the space and time units of the model) [28]. The resulting dimensionless reaction-diffusion model is as follows:

$$\frac{\partial U}{\partial t} = \mathrm{D}(\nabla^2 U) + \gamma\left[\frac{U^2}{(1+KU^2)V} - cU\right] \tag{3}$$

$$\frac{\partial V}{\partial t} = \nabla^2 V + \gamma(U^2 - eV + S) \tag{4}$$

The relationships between the dimensional and dimensionless parameters are:

$$x^* = \frac{x}{L},\ D = \frac{D_a}{D_h},\ t^* = \frac{D_h}{L^2}t,\ \gamma = \frac{L^2}{D_h}\gamma^*,\ U = \frac{c_a}{c_h}a,\ V = \frac{c_h\gamma^*}{c_a^2}h,\ K = \frac{c_a^2}{c_h^2}k,\ c = \frac{\mu_a}{\gamma^*},\ e = \frac{\mu_h}{\gamma^*},\ S = \frac{c_h}{c_a^2}H \tag{5}$$

The dimensionless model is used throughout this study because it removes dimensional units and simplifies parameter analysis. All subsequent numerical simulations in this study are based on this dimensionless model.

2.4 Mathematical analysis and numerical simulation

The prerequisite for pattern formation is that the system satisfies Turing instability, implying that the parameters must follow specific relationships and lie within certain ranges, which is referred to as the Turing space. A common method to obtain the Turing space is through Turing instability analysis. Here, we carefully consider the model parameters in the reaction-diffusion model (Equations (3-4)) to ensure the formation of patterns. The model includes dimensionless parameters *D*, γ, *K*, *c*, *e*, and *S*. Parameters *D*, *c*, and *e* mainly reflect intrinsic properties of the morphogen system, such as relative diffusion rates and degradation kinetics. These parameters are therefore fixed throughout the simulations to reduce parameter redundancy and maintain model identifiability. In contrast, parameters *K* and γ are variable and highly sensitive to pattern formation, making them ideal as key parameters for regulating pattern formation and transformation. *S* denotes a dimensionless exogenous inhibitor source term, where *S*=0 in the absence of exogenous inhibitor input in the experiment. We used Turing instability analysis and parameter scanning to determine the values of these two parameters.

The emergence of Turing patterns in the model requires the satisfaction of Turing instability conditions. In reaction-diffusion systems, spatial pattern formation arises from diffusion-driven instability [15]. Specifically, Turing instability requires that the homogeneous steady state remain stable in the absence of diffusion, but become unstable to spatial perturbations when diffusion is introduced. Accordingly, two fundamental conditions must be satisfied: (i) without diffusion, the homogeneous steady state is stable to small perturbations; (ii) with diffusion, this steady state becomes unstable to spatial perturbations, allowing perturbations with certain wavelengths to grow and eventually form stable spatially heterogeneous patterns. From a mechanistic perspective, this corresponds to the interplay between local self-activation and long-range inhibition. The activator promotes its own production locally, whereas the inhibitor suppresses activation over a larger spatial range because of its faster diffusion. Based on these conditions, we derive the parameter constraints for Turing instability in our model (see Equation (3)). The detailed derivation is provided in the Supplementary Information.

$$\left.\begin{aligned} f_U + g_V < 0 \Rightarrow K > [\tfrac{2}{1+r} - 1]\tfrac{1}{u_0^2} \\ f_U g_V - f_V g_U > 0 \Rightarrow \tfrac{1+3Ku_0^2}{1+Ku_0^2} > 0 \\ f_U + D g_V > 0 \Rightarrow K < [\tfrac{2}{1+Dr} - 1]\tfrac{1}{u_0^2} \\ (f_U + D g_V)^2 - 4D(f_U g_V - f_V g_U) > 0 \Rightarrow K < \left[\tfrac{2}{1-Dr+\sqrt{8Dr}} - 1\right]\tfrac{1}{u_0^2} \,\&\, \\ K > \left[\tfrac{2}{1-Dr-\sqrt{8Dr}} - 1\right]\tfrac{1}{u_0^2}, (1 - Dr \pm \sqrt{8Dr} > 0\ ) \end{aligned}\right\} \tag{3}$$

where f and g are the partial derivatives of the indicated variables, and $r = e/c$. The inequalities are evaluated in the steady state (u_0, v_0). Because $f(u_0, v_0) = 0$ and $g(u_0, v_0) = 0$, the steady-state values u_0 and v_0 are related to K, e, and c. Since the analytical expression of the steady-state solution u_0 is complicated, we treat u_0 as a parameter and vary it within a reasonable range (0.5 ~ 10). This range covers the admissible steady states for constructing the Turing instability region. Given D=0.005, the parameter space (Turing space) in which the system satisfies the Turing instability can be plotted as a function of K and r, as shown in Fig. 1a. For $r = e/c = 2$ (with e = 0.02, c = 0.01), we determined that the range of K is 0~0.3418.

We next investigated the parameters K and γ in the numerical simulation. As shown in Fig. 1b, when K is small, the system generates stable spot patterns, and when K gradually increases, the generated patterns gradually convert from spot patterns to stripe patterns. Fig. 1c shows that γ does not influence the pattern type, but higher γ leads to higher pattern density. We next found that a single-spot pattern is more likely when K is in the range of 0.005 to 0.011 and γ is between 170 and 210, as shown in Supplementary Fig. 5. In this work, we chose K = 0.01 and γ = 200 for single-spot pattern formation. The parameter selection for the double-spot pattern is described in detail in Section 3.3.

Based on time-lapse imaging, we selected the internal region encased by the zona pellucida of the oocyte as the target area for simulation, which corresponds to a circular region with a radius of ~33 μm. In the computer simulation, the 2D computing space is discretized uniformly into a 192×192 grid. To better approximate the cell shape, we selected a circular area with a radius of 90 units within the computing space as the simulation domain. Given that this radius corresponds to a physical length of 33 μm, hence $90L_1 = 33$ μm, giving a space unit of $L_1 = 0.36$ μm. Spindle formation in the time-lapse imaging takes ~300 min. In the model, the formation of the primary Turing single-spot pattern takes ~1.8×10^6 iterations, so setting $1.8\times10^6 T_1 = 300$ min yields a time unit of T_1=0.01 s. The finite-difference scheme was used for spatial discretization. The initial conditions of the activator (U) and inhibitor (V) were homogeneous distributions with 2% random disturbances in the simulation space to trigger system instability, which facilitates pattern formation. Our model was numerically simulated using a method with no-flux boundary conditions. The four-point Laplacian was applied for the diffusion operator.

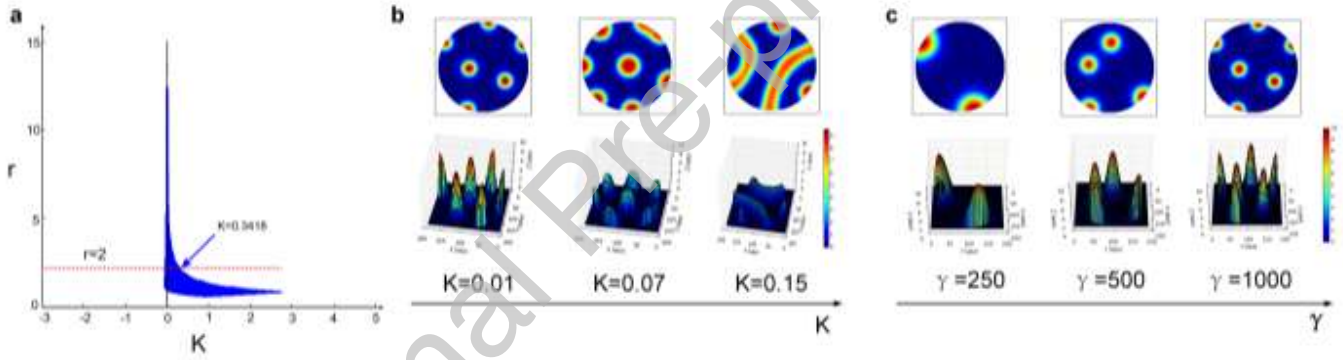

Fig. 1. Parameter selection of the reaction-diffusion mathematic model. a The parameter space of K and r indicates which combinations of parameter values lead to Turing patterns (blue region). Given r = 2, the parameter K has values of 0~0.3418 in the Turing space. **b** Patterns under different values of K. **c** Patterns under different values of γ. The 3D diagram shows the distribution of activators.

2.5 Dynamic characteristics

To determine the dynamic characteristics of the oocyte during maturation, we tracked the motion of the material inside the oocyte in each time-lapse image (video frame) and analyzed the tracking results. We used the HoughCircles function in OpenCV to identify the oocyte region (excluding zona pellucida) in an image before spindle formation. Then, we divided the oocyte region according to the pixels and selected sampling points every 10 pixels. To determine the motion of these sampling points, we employed an optical flow method, namely, the two-frame motion estimation method proposed by Farnebäck in 2003, to calculate the displacement of all sampling points between every two frames (frame N-1 and frame N) in two orthogonal directions [31]. We calculated the vector sum of the displacement in both directions and used the sum to represent the motion of a sampling point in frame N. The larger the motion between the two frames is, the higher the movement intensity of the sampling point. To assess the dynamic characteristics of the intracellular material during spindle formation and separation, we calculated the average motion of all sampling points in each frame to represent the movement intensity of that frame.

3. Results

3.1 Imaging of meiotic oocyte maturation

The construction of a mathematical model that describes spindle formation and separation requires a considerable amount of detailed information on oocyte meiosis. Currently, the spindle is typically observed through staining; however, the staining effect cannot be maintained for a long time, and oocytes may lose activity after staining and cannot continue developing. Thus, the most common approach is to culture many oocytes at the same time, stain a batch of cells to observe the spindle and obtain a frame of the spindle at a certain moment during the cell division process. However, variability among oocytes, the labor-intensive procedure, and the small number of available oocytes make it difficult to capture the complete developmental process with staining-based methods alone. Therefore, we used label-free time-lapse imaging to continuously monitor individual oocytes for tens of hours, allowing the spindle to be observed without exogenous markers. With this method, we observeed the complete maturation process of a meiotic oocyte without using fluorescent dyes, which facilitates subsequent analyses and modeling.

We recorded the entire meiotic oocyte maturation process using high-resolution DIC microscopy (Movie S1). Initially, as shown in Fig. 2a, the oocyte in the diplotene stage has a large internal nucleus with a clear boundary, which is known as the germinal vesicle (GV). GVBD occurs 1-1.5 hours after maturation, the well-defined GV within the oocyte gradually disappears, and no clear patterns emerge within the oocyte area. As shown in Fig. 2b, during a following longer period of time (approximately 5 hours), intracellular particles, such as chromosomes and microtubules, can move back and forth, possibly attempting to aggregate, resulting in spindle-like patterns. As shown in Fig. 2c, after the spindle has formed (approximately 6-8 hours after maturation), the spindle moves towards the cortex. As shown in Fig. 2d, the spindle rapidly separates while extruding a polar body. A detailed analysis of images acquired every 40 seconds shows that approximately 8 hours elapse from the start of GVBD to the initiation of anaphase I; however, only approximately 15 minutes elapse between anaphase I and the extrusion of the polar body. The DIC time-lapse imaging clearly indicates that spindle formation is considerably slower than spindle separation. (Movie S2 recorded the maturation process of the other mouse meiotic oocyte.)

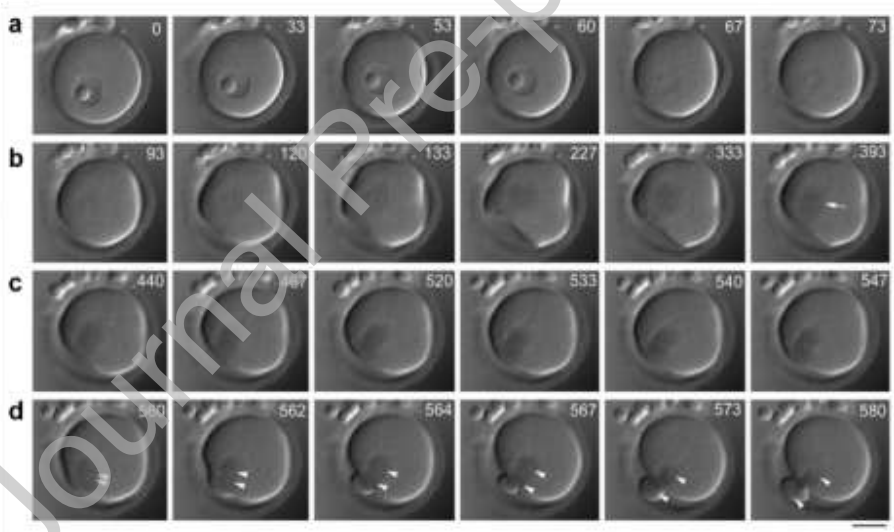

Fig. 2. Time-lapse images acquired with DIC microscopy. a Germinal vesicle breakdown occurs at 67 min. **b** Spindle formation, which takes about 5 h. The white arrow indicates the spindle (same below). **c** Migration of spindle from a central location to the cortex, which is completed within 2 h. **d** Spindle separation and oocyte extrusion of a polar body, which takes about 20 min. The number on the upper right corner indicates minutes since the start of recording (same below). Bar scale, 25 μm.

3.2 Mathematical model of spindle formation

We abstracted spindle formation (Fig. 2b) as a single-spot pattern and simulated it using the reaction-diffusion model. If the spindle formation process is regulated by Turing reaction-diffusion theory, the simulated results should closely align with the biological process, both in morphological characteristics and temporal dynamics. To enable a more precise morphological and temporal comparison, the simulation results were scaled to real-world time, with each iteration corresponding to 0.01 seconds (T_1=0.01 s), and then compared with the oocyte images at corresponding developmental stages in the time-lapse imaging (see Fig. 3a and b). After GVBD, no clear particle distribution patterns can be observed within the oocyte; accordingly, the initial state of morphogens was set as homogeneous. We set this moment as the initial simulation time, T=0, corresponding to minute 93 in the time-lapse imaging. Fig. 3a shows that by minute 227 (134 minutes after the minute 93) in the time-lapse imaging, an incipient

spindle structure is observable within the oocyte. Similarly, in Fig. 3b, at minute 134 of the simulation, morphogens accumulate within the simulation domain, exhibiting a trend towards forming a single-spot-like distribution. Finally, by minute 393 in the time-lapse imaging, the spindle structure is fully formed within the oocyte; similarly, in Fig. 3b, at minute 300 of the simulation, the single-spot pattern is formed within the computational domain. The results indicate that the simulated timeline, when mapped to real-world time, aligns well with the actual developmental timeline observed in the time-lapse imaging. The simulation shows strong spatiotemporal agreement with the spindle formation process observed in the time-lapse imaging, with no detectable phase lag.

Fig. 3c shows a 3D distribution of the activator, indicating that the activator is not uniformly distributed but instead exhibits a clear gradient, with high concentrations at the center that gradually decrease toward the periphery. Research has shown that the distribution of the activator represents a "chemical prepattern" that can direct the formation or transformation of biological patterns [32]. We speculate that certain proteins in the oocyte, similar to the activator, may establish a specific distribution, with higher concentrations at the center and lower concentrations at the periphery, guiding spindle formation in response to their influence. Notably, it has been reported that after GVBD, RanGTP forms a chromosome-centered gradient, as shown in Fig. 3d [12]. The gradient of RanGTP centered on chromosomes has been proposed not only to promote microtubule nucleation and spindle assembly but also to define the spatial domain and size of the spindle based on its single-spot-like distribution [6-12]. Interestingly, RanGTP and the activator exhibit highly similar distribution characteristics.

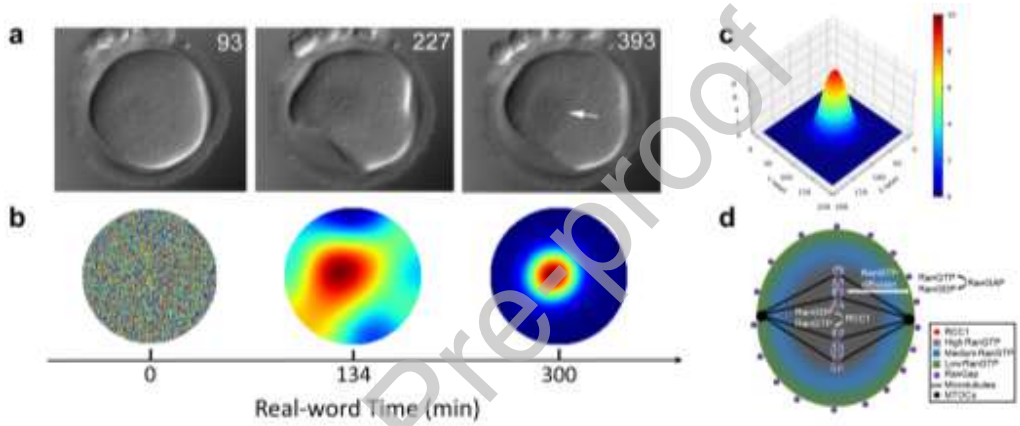

Fig. 3. Numerical simulation results of spindle formation. a Spindle formation observed in oocyte during time-lapse imaging (Movie S1), showing three stages: GVBD at minute 93, spindle assembly at minute 227, and the fully formed spindle at minute 393. **b** Single-spot pattern generated by the reaction-diffusion model (model parameter values: D=0.005, γ=200, K=0.01, c=0.01, H=0, e=0.02, S=0). The simulation results were mapped to real-world time (in minutes) based on the iteration count and the corresponding time unit T_1 = 0.01 s. Three key time points are presented: the simulation starting point T=0 corresponds to minute 93 in the imaging, the result after 8.04×10^5 iterations corresponds to minute 93 in the imaging, the result after 1.8×10^6 iterations represents minute 300 in simulation, which aligns with minute 393 in the imaging. **c** The 3D diagram shows the distribution of activators. **d** RanGTP gradient around MI spindle [12].

3.3 Mathematical model of spindle separation

After the spindle migrates to the cortex, the spindle quickly enters the separation stage, rapidly elongating and then splitting at the center, leading to the formation of the first polar body and the secondary oocyte. From the perspective of Turing theory, this process could be described as a pattern transformation, that is, the transformation from a single-spot pattern to a double-spot pattern.

The initiation of pattern transformation is typically attributed to the system losing stability due to certain factors, after which it gradually stabilizes under new conditions to form a new pattern. In this process, changes in specific parameters may be responsible for the loss of stability [13, 15, 16, 28]. Reference 33 demonstrated that the tuning parameter γ contributes to pattern transformation, inspiring us to explore the double-spot pattern by adjusting the parameter γ [33]. In the reaction-diffusion model, the parameter γ appears as a coefficient associated with the reaction terms and influences the effective reaction intensity of the system [15]. However, it should not be interpreted as a direct measure of biochemical reaction rates. Instead, γ represents an effective system-level parameter that characterizes the overall dynamical balance between reaction and diffusion processes.

To relate this parameter to the experimentally observed spindle dynamics, we used the optical flow method to analyze the dynamic characteristics of the two processes observed in Movie S1 separately, and the results showed that the spindle separation exhibits greater particle movement intensity compared to the spindle formation (the details of dynamic analysis were introduced in Section 3.4). Therefore, from the perspective of system reaction intensity, the updated parameter γ is likely greater than the γ of the single-spot pattern formation. To quantify the reaction intensity of the spindle formation and separation processes, we

calculated the average movement intensity of all particles in each frame of Movie S1, obtaining the average movement intensity curves of the spindle formation and separation respectively. These curves were then used as signals, and a fast Fourier transform was applied to obtain the spectrogram for each stage. The energy of each stage can be determined by integrating the amplitude over the frequency in the spectrogram. Supplementary Fig. 2 shows the spectrogram obtained from Movie S1, and we found that the ratio of the energy in the spindle separation to that in the spindle formation was 5.8. Rather than assuming a direct quantitative equivalence between this ratio and γ, we used it as a heuristic indicator of the change in the system's dynamical regime. Specifically, we increased γ proportionally (the updated γ is 1160) to reflect the transition from a low-activity (formation) to a high-activity (separation) state. The Note 2 of Supplementary Information shows the details.

If the spindle separation process is regulated by Turing reaction-diffusion theory, the simulated results should closely align with the biological process, both in morphological characteristics and in the temporal sequence of dynamic progression. Thus, prior to the numerical simulation, we need to estimate the time and space units for simulating spindle separation. Given that the simulation targets the spindle separation within the oocyte, specifically within the region bounded by the zona pellucida, the actual spatial scale of the simulation remains unchanged in this phase, so taking space unit $L_2 = L_1 = 0.36$ μm. As mentioned earlier, the parameter γ (defined as $\gamma = L^2\gamma^*/D_h$, where $\gamma^* = T^{-1}$) is scaled by a factor of 5.8. Given that the space unit L_2 and the diffusion coefficient D_h remain unchanged, the time unit is adjusted to 1/5.8 of its original value, so taking updated time unit $T_2 = 0.0017$ s.

We next employed the reaction-diffusion model to simulate spindle separation based on the Turing secondary pattern theory. To enable a more precise morphological and temporal comparison, the simulation results were scaled to real-world time, with each iteration corresponding to 0.0017 seconds, and then compared with the oocyte images at corresponding developmental stages in the time-lapse imaging, as shown in Fig. 4. At minute 547 after recording began, the spindle reaches the cortex in preparation for separation, marking the initial time point of the simulation ($T = 0$). At minute 562 (15 minutes after minute 547), a gradual elongation of the spindle was observed in the time-lapse imaging, similar to the elongated single-spot pattern shown at 15 minutes of simulation. After two minutes, the spindle elongation increased significantly, and it also showed a more obvious elongation trend at minute 17 of simulation. As time progresses, continued elongation of the spindle is accompanied by a gradual formation of a new cell membrane at the center; likewise, in the simulation, two morphogen peaks shift in opposite directions, with concentrations between them decreasing and approaching zero. Finally, at minute 580 in the imaging (33 minutes after minute 547), the spindle split into two parts, forming the secondary oocyte and polar body. Correspondingly, the simulation at minute 33 also shows the formation of the double-spot pattern, with the spots becoming no longer connected. The results demonstrate strong spatiotemporal agreement between the numerical simulation and the spindle separation process observed in the time-lapse imaging, with no detectable phase lag.

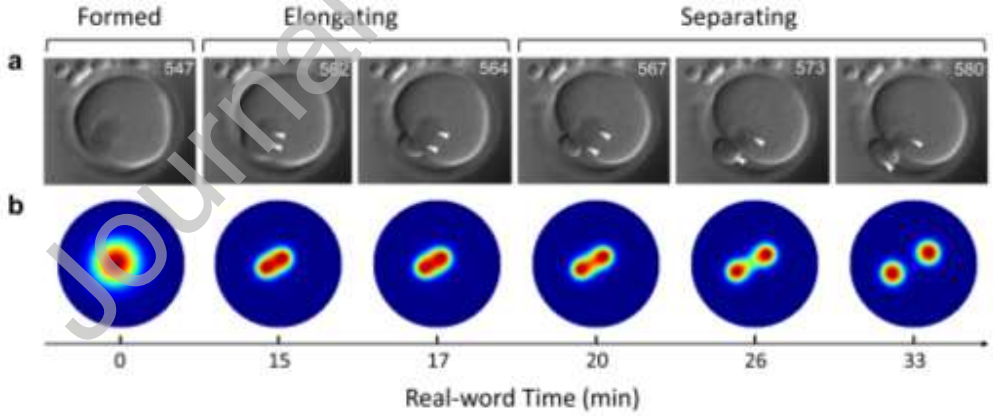

Fig. 4. Numerical simulation results of spindle separation. a Spindle separation observed in oocyte during time-lapse imaging (Movie S1), showing six critical moments: the spindle reaches the cortex at minute 547 and quickly enters the separation stage, rapidly elongating (minutes 562 and 564) and then splitting at the center (minutes 567, 573, and 580), leading to the formation of the first polar body and the secondary oocyte. **b** Double-spot pattern generated from the preceding single-spot pattern, based on the secondary pattern predicted by Turing theory (model parameter values: D=0.005, γ=1160, K=0.01, c=0.01, H=0, e=0.02, S=0). The simulation results were mapped to real-world time (in minutes) based on the iteration count and the corresponding time unit $T_2 = 0.0017$ s. Six critical time points are presented: the simulation starting point T=0 corresponds to minute 547 in the time-lapse imaging; results after 5.22×10^5 and 5.916×10^5 iterations illustrate single spot elongation, corresponds to minute 562 and minute 564 in the imaging, respectively; As iterations progress, the elongated single spot gradually splits at the center; the result after 1.15×10^6 iterations shows a clear formation of the double-spot pattern, representing minute 33 in the simulation, which aligns with minute 580 in the imaging.

3.4 Dynamic characteristics analysis

In modeling biological pattern formation using Turing theory, morphological similarity is a critical evaluation criterion. Moreover, we believe that the dynamics of pattern formation are equally important to investigate. Here, we analyzed the dynamic characteristics of spindle formation and separation observed in Movie S1 and pattern formation processes in the numerical simulations to assess whether they exhibit similar characteristics. We selected sampling points within the region of the oocyte in Movie S1 and employed the optical flow method to obtain the displacement of all sampling points between every two frames, allowing us to assess movement intensity at each sampling point, with color indicating different levels of intensity.

The experimental time-lapse imaging. As shown in Fig. 5a, spindle formation involves a low-intensity process, and Fig. 5b shows that the particles inside the oocyte have higher movement intensity during spindle separation. To quantify the dynamic characteristics of those two processes, we calculated the average movement intensity of all sampling points in each frame and plotted a time-based line chart of this average movement intensity. During spindle formation, as shown in the blue region of the line chart in Fig. 5c, the particle movement intensity is around 0.25 and decreases to approximately 0.1 once the spindle has fully formed. In the spindle separation phase, represented in the orange region of Fig. 5c, the movement intensity increases significantly to a peak of approximately 1.7, then decreases to 0.5 following the extrusion of the first polar body. Moreover, the inserted violin plots illustrate the distribution of the movement intensity of the sampling points in a selected frame, highlighting the difference in the movement intensity within the oocyte. The three violin plots in the blue part of Fig. 5c indicate minimal differences in particle movement intensity across different parts of the oocyte during spindle formation. In contrast, the violin plots in the orange region reveal a significant difference in movement intensity within localized regions of the oocyte during spindle separation, indicating that certain areas are undergoing significantly more vigorous activity than others.

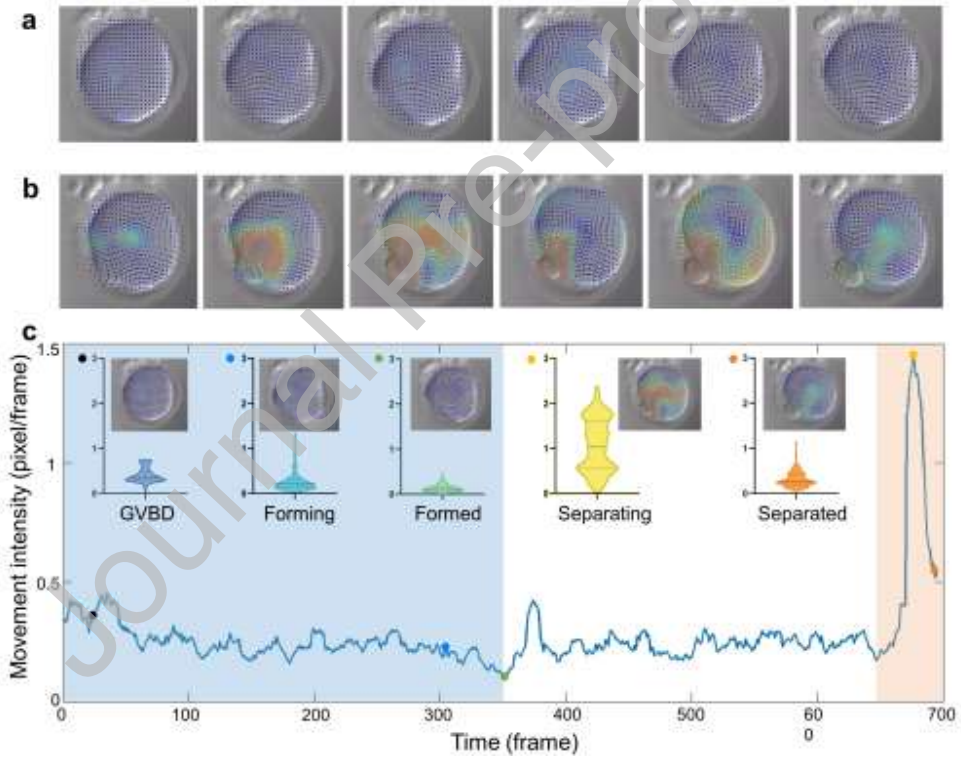

Fig. 5. Dynamic analysis of spindle formation and separation. a Sampling points in Fig. 2b were tracked using the optical flow method, with color representing movement intensity, ranging from blue (low) to red (high). **b** Sampling points in Fig. 2d were tracked by the optical flow method. **c** Average value of the particle movement intensity in each frame from spindle formation to spindle separation (blue area: spindle formation; orange area: spindle separation; remaining white area: spindle migration to the cortex). The insets show violin plots illustrating the distribution of movement intensities for all sampling points within the oocyte.

The numerical simulations. We used the same method to analyze the dynamic characteristics of the simulation results. As shown in Fig. 6a, single-spot pattern formation involves a low-intensity process. As shown in Fig. 6b, transforming from a single-spot to a double-spot pattern involves a high-intensity process. In quantitative terms, the blue region of the line chart in Fig. 6c indicates that during the formation of the single-spot pattern, particle movement intensity peaks at approximately 0.025 and decreases to 0 once the pattern has fully formed. During the pattern transformation, after γ is tuned, the orange region shows a rapid increase in particle movement intensity, peaking at around 0.07, before decreasing to nearly 0 as the double-spot pattern forms.

We next compared the dynamic characteristics of the numerical simulation results with those of time-lapse imaging. Overall, during the formation of the double-spot pattern, the particle movement intensity was significantly higher than that during the single-spot pattern formation (Fig. 6c), aligning with the observed greater movement intensity during spindle separation compared to spindle formation (Fig. 5c). In terms of dynamic trends, a sharp increase in particle movement intensity is observed at the onset of double-spot pattern formation, whereas during single-spot formation, the particle movement intensity remains at a low level (Fig. 6c). This parallels the observation that, at the start of spindle separation, movement intensity rises significantly, while during spindle formation, it varies within a smaller range (Fig. 5c). Regarding the distribution of particle dynamics, notable differences in movement intensity were observed among various regions during the spindle separation/double-spot pattern formation processes. In contrast, movement intensity differences were moderate during the spindle formation/single-spot pattern formation phase. The movement intensity values in the experiments and simulations differ significantly, mainly due to differences in image resolution, background motion in the experimental data, and temporal sampling intervals. However, the overall dynamic trends show good consistency, supporting the ability of the reaction-diffusion model to reproduce the processes of spindle formation and separation.

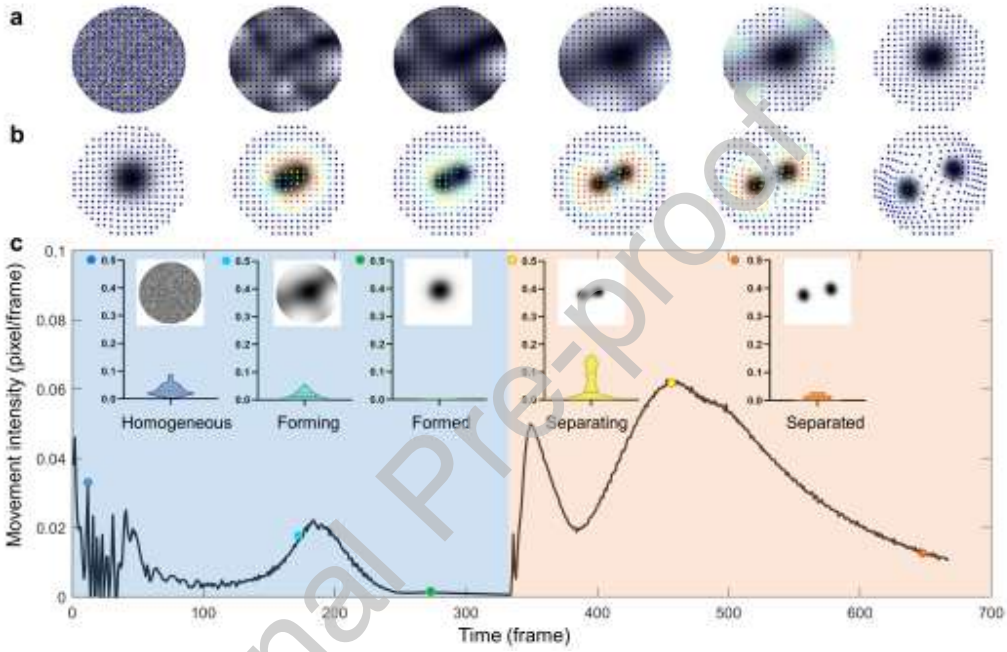

Fig. 6. Dynamic analyses of simulation results. Sampling points in the simulation area tracked by the optical flow method during **a** single-spot pattern formation and **b** double-spot pattern formation. **c** Average particle movement intensity during single-spot pattern and double-spot pattern formation in the simulation results (blue area: single-spot formation stage; orange area: double-spot formation stage). The insets show violin plots of the sampling point motilities in five keyframes, corresponding to Fig. 5c.

3.5 Reaction-diffusion model predictions and experimental tests

The reaction-diffusion model predicts how an increase in inhibitory input affects spindle separation dynamics. As shown in Fig. 7a, the introduction of an exogenous inhibitor source term (S) significantly affects the secondary pattern formation process. Specifically, as S increases, the transformation from a single-spot pattern to a double-spot pattern is progressively delayed and may eventually be completely suppressed. From the perspective of the model, S acts as an exogenous source term that directly determines the baseline level of the inhibitor field. It shifts the spatially homogeneous steady state of the system, thereby altering the balance between activation and inhibition and affecting pattern transformation. In this study, S is interpreted as an exogenous input of inhibitory influence, representing an increase in the overall inhibitory strength at the system level. Accordingly, the model yields two predictions: increased inhibitory input (i.e., increasing S) (i) reduces the separation potential of the spindle, and (ii) prolongs the duration of spindle separation.

To experimentally examine these predictions, we employed importazole (IPZ), which has been reported to disrupt spindle-related processes by Jonathan et al. [34], to simulate the increased inhibitory input in the system. Rather than directly increasing the concentration of a specific inhibitory molecule, IPZ treatment reduces the effective activity of spindle-related processes and thus enhances the overall inhibitory influence at the system level. In this sense, IPZ provides a functional realization of an increased inhibitory input, consistent with the role of the source term S in the model.

To design the validation experiments, we first conducted preliminary observations under our laboratory conditions, observing that spindle separation usually begins after about 8 hours of in vitro culture and is basically completed in about 10 hours (Supplementary Information shows experimental details).

The first prediction was that increased inhibitory input would reduce the separation potential of the spindle. To support this prediction, we started culturing GV cells in vitro at *T*=0 h, and at *T*=6h, we treated 23 meiosis I metaphase oocytes with 200 μM IPZ for seven hours. As shown in Fig. 7b, at *T*=13h, only 39.13% of the oocytes in the IPZ treatment group entered meiosis II (complete separation), while 66.67% of the 22 oocytes in the control group entered meiosis II. This indicates a reduced number of IPZ-treated oocytes successfully progressing to meiosis II, suggesting that increased inhibitory input likely reduces the separation potential of the spindle.

The second prediction was that increased inhibitory input would prolong the duration of spindle separation. To support this prediction, we started culturing GV cells in vitro at *T*=0 h, and we treated 36 oocytes with 200 μM IPZ at *T*=6 h. As shown in Fig. 7c, at *T*=7 h, more than 80% of the oocytes (both IPZ-treated oocytes and the 30 control oocytes) were in metaphase I and anaphase I; while at *T*=9 h, all the oocytes in the IPZ treatment group were still in meiosis I, whereas 20% of oocytes in the control group had reached meiosis II. This result shows that IPZ-treated oocytes, unlike control oocytes, did not enter meiosis II by *T* = 9 h and may require more time to complete separation (see the verification experiment for Prediction 1). This suggests that increased inhibitory input likely prolongs the duration of spindle separation.

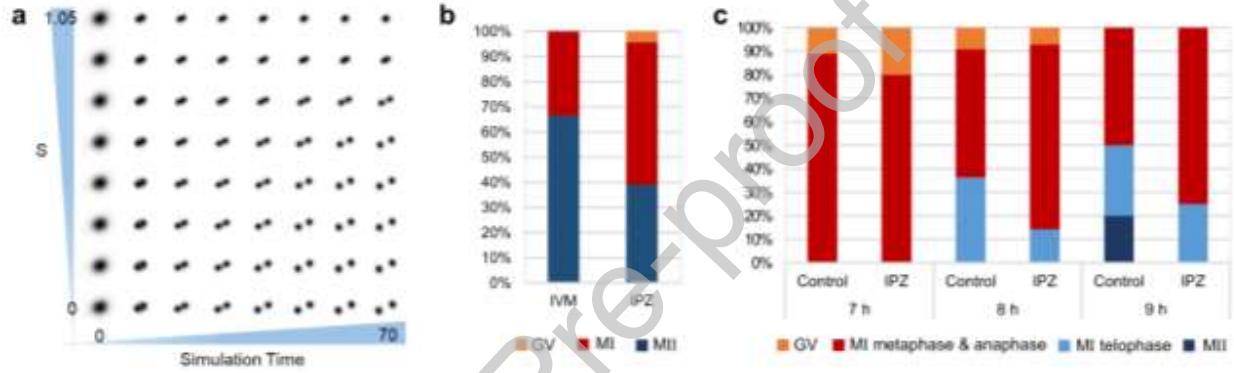

Fig. 7. Predictions of the reaction-diffusion model and experimental tests. a Numerical simulation results of spindle separation with an abnormally increasing inhibitor. To simulate increased inhibitory input, we increased the exogenous source term *S* from 0 to 1.05. **b** The effect of IPZ on the rate of successful spindle separation. Meiosis I metaphase oocytes were collected after 7 hours of IVM culture, and then treated with 200 μM IPZ for seven hours, and fixed and stained for tubulin and chromosomes. In the IPZ treatment group, 39.13% of the oocytes reached meiosis II metaphase; in the control group, 66.67% of the oocytes reached meiosis II. **c** The effect of IPZ on the duration of spindle separation. Meiosis I metaphase oocytes were collected after in vitro maturation (IVM) culture for 6 hours, and then some of them treated with 200 μM IPZ for either one hour, two hours or three hours and fixed and stained for tubulin and chromosomes. We defined oocytes that reached meiosis I telophase or meiosis II as having successfully separated spindles. One hour after the treatment, we found that most oocytes in both the IPZ treatment and control groups were in meiosis I metaphase. However, after two hours, fewer oocytes had undergone meiosis I telophase in the IPZ treatment group than in the control group (14.29% vs. 36.36%). After three hours, 25% of IPZ-treated oocytes completed spindle separation and remained at meiosis I telophase, while 50% of the oocytes arrived at meiosis I telophase or even meiosis II metaphase in the control medium.

4. Discussion and conclusion

In this study, we used a Turing reaction-diffusion model to simulate spindle formation and separation based on Turing secondary pattern theory, with the goal of providing a new perspective on understanding these two critical biological processes. Firstly, we recorded mouse oocyte spindle formation and separation by DIC microscopy without injecting dyes or fluorescent proteins. From a pattern formation perspective, spindle formation was abstracted as the development of a single-spot primary Turing pattern, while spindle separation was abstracted as the transformation of this primary pattern into a double-spot secondary Turing pattern. In the numerical simulations, starting from a homogeneous state that biologically corresponds to the period shortly after GVBD before spindle formation, the model generated a single-spot pattern, replicating the spindle formation process. Based on Turing theory, this initial pattern underwent rapid changes through key parameter adjustments, ultimately splitting into a stable double-spot pattern, simulating the spindle separation process. Notably, the simulation results and time-lapse imaging exhibited strong spatiotemporal agreement across morphological features and developmental timescales, with no detectable phase lag. Subsequently, we applied optical flow analysis to compare the dynamic characteristics of the time-lapse imaging and numerical simulations, revealing a consistent trend in their particle movement intensity. Finally, the model provided two predictions: increased inhibitory input (i) would reduce the separation potential of the spindle, and (ii) would prolong the duration of spindle

separation. The following cell experiments supported the model predictions. These findings suggest that Turing reaction-diffusion principles may be involved in the regulation of spindle formation and separation.

In this study, we performed DIC microscopy imaging without injecting dyes or fluorescent proteins to obtain the details of oocyte meiosis without disturbing oocyte activity. In this way, we could observe the details of oocyte development, enabling more detailed and more accurate monitoring. Moreover, in addition to the spindle, other regions of the oocyte could be recorded. The detailed movies allowed us to evaluate the dynamic characteristics of the pattern formation process to determine whether the mathematical model is consistent with the process in the cell. The improved time-lapse imaging techniques, which do not require the microinjection of dyes or fluorescent proteins, may be valuable tools in further studies.

There have been mathematical modeling studies on spindle formation or separation, which consider the influence of many specific key factors. For example, Stuart C. et al. proposed a biophysical model to explore the mechanisms of spindle pattern formation by modeling the role of motor proteins, particularly Eg5 and chromatin-driven motors, in microtubule assembly during spindle formation [35]. Changji Shi et al. constructed a model based on microtubule polymerization, RanGTP/RanGDP conversion, and the role of lamin-B protein, and the simulation results were consistent with experimental observations [36]. Cytrynbaum et al. used a force balance model to describe the distribution of microtubules and dynein and the role of forces, which accurately predicts the relationship between force and pole separation distance [37]. These studies provide complementary explanations from different perspectives and are not in conflict with the reaction-diffusion interpretation proposed here. However, organismal development always occurs as a sequential process, where pattern transformation is more frequent than primary pattern emergence from a homogeneous state. In this study, we considered the formation and separation of spindles as a transformation from primary to secondary patterns in the same basic theoretical framework. The connection between those two spindle development processes has been considered rather than focused on only a single process (spindle formation or separation). Although our model does not account for certain specific structures involved in spindle formation and separation, such as actin, it provides a systems-level interpretation of these processes that may offer valuable insights for future biological research.

Beyond the morphological comparisons typical of reaction–diffusion studies, we further investigated the dynamic characteristics of biological and simulation processes. Specifically, based on optical flow method, we analyzed the dynamic characteristics of four processes: spindle formation and separation, as well as the emergence of single-spot and double-spot patterns in the numerical simulations. The dynamic characteristics of pattern formation and transformation closely match those from time-lapse imaging. Particle movement intensity rises from a low level during spindle formation (single-spot pattern) to a high level during separation (double-spot pattern), a trend observed consistently in the simulations and in the time-lapse imaging. This evaluation provides additional support for validating the model in addition to the typical criteria (such as the morphological similarity of the initial conditions and the resulting patterns).

Furthermore, based on the dynamic characteristics of biological processes, we derived the key parameter γ that facilitates the transformation from single-spot to double-spot pattern. Here, we discuss the validity of the approach used to determine this parameter. As mentioned in Section 3.3, we updated the γ value to 5.8 times its original value based on the energy ratio between the separation and formation phases, yielding 1160, which was capable of producing the double-spot pattern in simulations. Subsequently, we conducted a parameter scanning around this updated value to determine the γ range that generates a double-spot pattern in simulations, which was found to be between 900 and 1600 (see Supplementary Fig. 6). We then performed the same dynamic characteristic analysis on Video S2, which revealed an energy ratio of 7.11 between the spindle separation and formation phases (see Supplementary Figure 3). The resulting updated γ value is 1422, which falls within the previously identified range of γ values (900 to 1600). Although this method can estimate changes in the parameter γ, it relies heavily on the stability of the time-lapse imaging and the imaging angle. Severe occlusion or camera shake can introduce errors in optical flow detection, resulting in inaccurate energy ratio calculations and, consequently, incorrect parameter estimates. Despite these limitations, we believe that using optical flow to capture the dynamic characteristics of biological development and to identify model parameters from these dynamics is a promising approach. We note that the principle of estimating system parameters from observed pattern dynamics has also been explored in other contexts, including reaction–diffusion models of epidemic and information propagation [38-40].

The model used in this study is a coarse-grained, system-level representation whose core purpose is to capture the overall spatiotemporal dynamics of spindle formation and separation through activator–inhibitor interactions. It does not explicitly include specific biomechanical or biochemical details, such as microtubule mechanics, motor-protein interactions, or actin-mediated forces, nor does it fully reproduce certain geometric features observed in the experiments. Because the parameters are coarse-grained and not linked to specific molecules, the model serves as a system-level framework for pattern organization rather than a molecular mechanistic description. Incorporating additional biophysical mechanisms and establishing closer links between model parameters and molecular processes are important directions for future refinement.

The identification of morphogens is an important step in explaining the formation of biological patterns using the Turing model. Building on prior biological studies, we propose potential candidates for the morphogens involved in our model. After GVBD, RanGTP forms a gradient distribution centered on chromosomes, which has been proposed not only to promote microtubule nucleation and spindle assembly but also to define the spatial domain and size of the spindle based on its distribution

[6-12]. Even in the absence of centromeres, the RanGTP gradient continues to play a crucial role during meiosis by activating the microtubule factors necessary for spindle formation. As shown in Fig. 3d, following GVBD, Chromosome Condensation Factor 1 (RCC1), which is linked to the chromosomes, becomes exposed in the cytoplasm and regulates the formation of the RanGTP gradient. RCC1 is a guanine nucleotide exchange factor, facilitating the conversion of RanGDP to RanGTP. This continuous conversion results in a higher concentration of RanGTP near the nuclear material, while spatial diffusion of RanGTP creates a gradient distribution around it. RanGTP is crucial for microtubule nucleation during spindle formation [12]. This is because RanGTP induces spindle formation by binding to inhibitory proteins (such as Importin-α and Importin-β) and regulating the release of substances that contribute to spindle assembly (such as TPX2 and NuMA) [11, 41]. RanGTP regulates over 22 factors involved in spindle assembly during mitosis, which play crucial roles in processes such as microtubule nucleation, stabilization, bundling, elongation, protective transport along microtubules, accumulation at the spindle poles, and γ-tubulin localization [10, 42]. As RanGTP diffuses within the cell, RanGAP in the cytoplasm activates RanGTPase, catalyzing the conversion of RanGTP to RanGDP, which leads to a decrease in the RanGTP concentration at that region. The interconversion between RanGTP and RanGDP creates the gradient field shown in Fig. 4b, which delineates the region for spindle formation and facilitates the assembly of the spindle. The interconversion process between RanGTP and RanGDP, catalyzed by related factors, resembles the morphogen reaction-diffusion process described in our model (Equations (1-2)). Moreover, the concentration gradient of RanGTP aligns well with our simulation results (Fig. 4a). Therefore, we interpret RanGTP as a functional analogue of the activator and RanGDP as a functional analogue of the inhibitor in our reaction-diffusion model. We emphasize that this mapping is intended to capture the essential features of the observed pattern formation, rather than to establish a direct quantitative correspondence between model variables and specific molecular concentrations. We cannot exclude the possibility that other gene products may act as morphogens, and further experimental validation will be valuable to refine this interpretation.

In conclusion, our study suggests that Turing reaction-diffusion theory may offer a potential explanation for spindle formation and separation during oocyte meiosis. Both the morphology and dynamic characteristics of these processes can be reproduced by the model, offering a framework for understanding the spatial organization of regulatory factors. Beyond normal dynamics, the model offers a system-level perspective on spindle-related abnormalities. For example, simulated behaviors such as failed or delayed pattern transformation, or unstable double-spot patterns, may correspond to defects in spindle assembly during oocyte meiosis, which may further lead to chromosome mis-segregation, thereby increasing the risk of aneuploidy. Furthermore, based on our label-free DIC imaging and optical-flow-based dynamic analysis, the cellular dynamic characteristics can be quantified in real time and linked to the key parameter γ for pattern transformation in the model. This connection enables model-based prediction of the spindle behavious, providing a potential non-invasive method for assessing oocyte quality and identifying abnormal developmental conditions.

Acknowledgment

The work described in this paper was supported by grants from the National Natural Science Foundation of China (62333012). During the preparation of this work the authors used DeepSeek for language refinement, grammar correction, and improving the conciseness of the manuscript. After using this tool, the authors reviewed and edited the content as needed and take(s) full responsibility for the content of the published article.

References

[1] T. Hassold, P. Hunt, To err (meiotically) is human: the genesis of human aneuploidy, Nat Rev Genet, 2 (2001) 280-291.
[2] J. Guo, T. Zhang, Y. Guo, T. Sun, H. Li, X. Zhang, H. Yin, G. Cao, Y. Yin, H. Wang, L. Shi, X. Guo, J. Sha, J.J. Eppig, Y.Q. Su, Oocyte stage-specific effects of MTOR determine granulosa cell fate and oocyte quality in mice, Proc Natl Acad Sci U S A, 115 (2018) E5326-e5333.
[3] L. Liu, R. Oldenbourg, J.R. Trimarchi, D.L. Keefe, A reliable, noninvasive technique for spindle imaging and enucleation of mammalian oocytes, Nat Biotechnol, 18 (2000) 223-225.
[4] C. So, K.B. Seres, A.M. Steyer, E. Mönnich, D. Clift, A. Pejkovska, W. Möbius, M. Schuh, A liquid-like spindle domain promotes acentrosomal spindle assembly in mammalian oocytes, Science, 364 (2019).
[5] E. Vogt, M. Kirsch-Volders, J. Parry, U. Eichenlaub-Ritter, Spindle formation, chromosome segregation and the spindle checkpoint in mammalian oocytes and susceptibility to meiotic error, Mutat Res, 651 (2008) 14-29.
[6] R. Bayliss, T. Sardon, I. Vernos, E. Conti, Structural basis of Aurora-A activation by TPX2 at the mitotic spindle, Mol Cell, 12 (2003) 851-862.
[7] S. Brunet, J. Dumont, K.W. Lee, K. Kinoshita, P. Hikal, O.J. Gruss, B. Maro, M.H. Verlhac, Meiotic regulation of TPX2 protein levels governs cell cycle progression in mouse oocytes, PLoS One, 3 (2008) e3338.
[8] J. Dumont, S. Petri, F. Pellegrin, M.E. Terret, M.T. Bohnsack, P. Rassinier, V. Georget, P. Kalab, O.J. Gruss, M.H. Verlhac, A centriole- and RanGTP-independent spindle assembly pathway in meiosis I of vertebrate oocytes, J Cell Biol, 176 (2007) 295-305.
[9] P. Kaláb, P. Solc, J. Motlík, The role of RanGTP gradient in vertebrate oocyte maturation, Results Probl Cell Differ, 53 (2011) 235-267.
[10] T. Cavazza, I. Vernos, The RanGTP Pathway: From Nucleo-Cytoplasmic Transport to Spindle Assembly and Beyond, Front Cell Dev Biol, 3 (2015) 82.

[11] L.N. Weaver, C.E. Walczak, Spatial gradients controlling spindle assembly, Biochem Soc Trans, 43 (2015) 7-12.
[12] A.L. Severance, K.E. Latham, Meeting the meiotic challenge: Specializations in mammalian oocyte spindle formation, Mol Reprod Dev, 85 (2018) 178-187.
[13] A.M. Turing, The Chemical Basis of Morphogenesis, Bulletin of Mathematical Biology, 237 (1952) 37-72.
[14] H. Meinhardt, Models of Biological Pattern Formation, Abstr Pap Am Chem S, 22 (1982).
[15] J.D. Murray, Mathematical Biology II : Spatial Models and Biomedical Applications, Springer-Verlag2003.
[16] A. Yochelis, Y. Tintut, L. Demer, A. Garfinkel, The formation of labyrinths, spots and stripe patterns in a biochemical approach to cardiovascular calcification, New Journal of Physics, 10 (2008).
[17] A. Gierer, H. Meinhardt, A theory of biological pattern formation, Kybernetik, 12 (1972) 30-39.
[18] M.P. Harris, S. Williamson, J.F. Fallon, H. Meinhardt, R.O. Prum, Molecular evidence for an activator–inhibitor mechanism in development of embryonic feather branching, Proc Natl Acad Sci U S A, 102 (2005) 11734-11739.
[19] A.R. Sanderson, R.M. Kirby, C.R. Johnson, L. Yang, Advanced Reaction-Diffusion Models for Texture Synthesis, Journal of Graphics GPU and Game Tools, 11 (2006) 47-71.
[20] Meinhardt, Hans, The algorithmic beauty of sea shells, The algorithmic beauty of sea shells2009.
[21] H. Fujita, K. Toyokura, K. Okada, M. Kawaguchi, Reaction-diffusion pattern in shoot apical meristem of plants, PLoS One, 6 (2011) e18243.
[22] C.W. Cheng, B. Niu, M. Warren, L.H. Pevny, R. Lovell-Badge, T. Hwa, K.S. Cheah, Predicting the spatiotemporal dynamics of hair follicle patterns in the developing mouse, Proc Natl Acad Sci U S A, 111 (2014) 2596-2601.
[23] L. Zhu, T. Zheng, Pattern dynamics analysis and application of West Nile virus spatiotemporal models based on higher-order network topology, Bulletin of Mathematical Biology, 87 (2025) 121.
[24] L. Zhu, Y. Li, Dynamic propagation and control of a West Nile virus model based on higher-order temporal network structure, Physical Review E, 112 (2025) 044409.
[25] B. Li, L. Zhu, Turing instability analysis of a reaction–diffusion system for rumor propagation in continuous space and complex networks, Information Processing and Management, 61 (2024) 103621.
[26] S. Dai, L. Zhu, L. He, Y. Dong, Dynamics and control of infectious diseases on complex networks: a theoretical and empirical study, Journal of Mathematical Analysis and Applications, 557 (2025) 130334.
[27] H. Meinhardt, P.A. de Boer, Pattern formation in Escherichia coli: a model for the pole-to-pole oscillations of Min proteins and the localization of the division site, Proc Natl Acad Sci U S A, 98 (2001) 14202-14207.
[28] A. Garfinkel, Y. Tintut, D. Petrasek, K. Boström, L.L. Demer, Pattern formation by vascular mesenchymal cells, Proc Natl Acad Sci U S A, 101 (2004) 9247-9250.
[29] Y. Fu, M. Sun, X. Zhao, S. Guo, A novel way for microvascular network pattern formation based on a pre-pattern guidance mechanism, Chaos, Solitons & Fractals, 186 (2024) 115322.
[30] Y. Guo, T.H. Chen, X. Zeng, D. Warburton, K.I. Boström, C.M. Ho, X. Zhao, A. Garfinkel, Branching patterns emerge in a mathematical model of the dynamics of lung development, The Journal of physiology, 592 (2014) 313-324.
[31] G. Farnebäck, Two-Frame Motion Estimation Based on Polynomial Expansion, 13th Scandinavian Conference on Image Analysis (SCIA 2003), Berlin, Heidelberg, Springer, 2003, pp. 363–370..
[32] S. Kondo, T. Miura, Reaction-diffusion model as a framework for understanding biological pattern formation, Science, 329 (2010) 1616-1620.
[33] R. Sheth, L. Marcon, M.F. Bastida, M. Junco, L. Quintana, R. Dahn, M. Kmita, J. Sharpe, M.A. Ros, Hox Genes Regulate Digit Patterning by Controlling the Wavelength of a Turing-Type Mechanism, Science, 338 (2012) 1476.
[34] J.F. Soderholm, S.L. Bird, P. Kalab, Y. Sampathkumar, K. Hasegawa, M. Uehara-Bingen, K. Weis, R. Heald, Importazole, a small molecule inhibitor of the transport receptor importin-β, ACS Chem Biol, 6 (2011) 700-708.
[35] S.C. Schaffner, J.V. José, Biophysical model of self-organized spindle formation patterns without centrosomes and kinetochores, Proc Natl Acad Sci U S A, 103 (2006) 11166-11171.
[36] C. Shi, W.E. Channels, Y. Zheng, P.A. Iglesias, A computational model for the formation of lamin-B mitotic spindle envelope and matrix, Interface Focus, 4 (2014) 20130063.
[37] E.N. Cytrynbaum, J.M. Scholey, A. Mogilner, A Force Balance Model of Early Spindle Pole Separation in Drosophila Embryos, Biophysical Journal, 84 (2003) 757-769.
[38] T. Yang, L. Zhu, S. Shen, L. He, Pattern dynamics analysis and parameter identification of spatiotemporal infectious disease models on complex networks, Mathematical Biosciences, 387 (2025) 109502.
[39] L. Zhu, Y. Ding, S. Shen, Green behavior propagation analysis based on statistical theory and intelligent algorithm in data-driven environment, Mathematical Biosciences, 379 (2025) 109340.
[40] H. Sha, L. Zhu, Dynamic analysis of pattern and optimal control research of rumor propagation model on different networks, Information Processing and Management, 62 (2025) 104016.
[41] O.J. Gruss, R.E. Carazo-Salas, C.A. Schatz, G. Guarguaglini, J. Kast, M. Wilm, N. Le Bot, I. Vernos, E. Karsenti, I.W. Mattaj, Ran induces spindle assembly by reversing the inhibitory effect of importin α on TPX2 activity, Cell, 104 (2001) 83-93.
[42] C.E. Walczak, R. Heald, Mechanisms of mitotic spindle assembly and function, International review of cytology, 265 (2008) 111-158.

Supporting information

S1 Text. Supporting information file containing tutorials and supplemental supplementary Figs 1-9. The Supporting Information is divided into several sections: Supplementary Note 1 introduces the validation experiments of model predictions;

Supplementary Note 2 explains the dynamic characteristics in detail; Supplementary Note 3 shows the mathematical conditions to satisfy the Turing instability; Supplementary Note 4 shows the p arameter selection supplementary information; Supplementary Note 5 shows the numerical perturbation tests.

S2 Movies. Supporting Movies containing 5 separate files. Movie S1-S2 are meiotic oocyte maturation processes recorded in mice by high-resolution DIC imaging. Movie S3 shows movement intensity of sampling points in Movie S1. Movie S4 shows numerical simulation results of spindle formation and separation stages. Movie S5 shows movement intensity of sampling points in Movie S4.

Declaration of interests

☐ The authors declare that they have no known competing financial interests or personal relationships that could have appeared to influence the work reported in this paper.

☒ The authors declare the following financial interests/personal relationships which may be considered as potential competing interests:

Xin Zhao reports financial support was provided by National Natural Science Foundation of China. If there are other authors, they declare that they have no known competing financial interests or personal relationships that could have appeared to influence the work reported in this paper.